Available online at www.sciencedirect.com

SciVerse ScienceDirect

Ceramics International 38 (2012) 2059–2064

CERAMICS INTERNATIONAL

www.elsevier.com/locate/ceramint

Facile synthesis and X-ray peak broadening studies of $Zn_{1-x}Mg_xO$ nanoparticles

A. Khorsand Zak [a,*], Ramin Yousefi [b], W.H. Abd Majid [a], M.R. Muhamad [c]

[a] Low Dimensional Material Research Center, Department of Physics, Faculty of Science, University of Malaya, 50603 Kuala Lumpur, Malaysia
[b] Department of Physics, Masjed-Soleiman Branch, Islamic Azad University (I.A.U), Masjed-Soleiman, Iran
[c] Chancellery, University of Multimedia, Cyberjaya Campus, 63100 Cyberjaya, Selangor, Malaysia

Received 18 June 2011; received in revised form 15 October 2011; accepted 18 October 2011
Available online 23 October 2011

Abstract

Magnesium-doped ZnO nanoparticles (NPs) ($Zn_{1-x}Mg_xO$-NPs, $x = 0.0, 0.01, 0.03$, and 0.05) were synthesized by a simple sol–gel method. The compounds were synthesized at calcination temperatures of 650 °C for 2 h. The synthesized $Zn_{1-x}Mg_xO$-NPs were characterized by X-ray diffraction analysis (XRD) and high-magnification transmission electron microscopy (TEM). The XRD results revealed that the sample product was crystalline with a hexagonal wurtzite phase. The TEM showed $Zn_{1-x}Mg_xO$-NPs with nearly spherical and hexagonal shapes. The size–strain plot (SSP) method was used to study the individual contributions of crystallite sizes and lattice strain on the peak broadening of the $Zn_{1-x}Mg_xO$-NPs. Physical parameters such as strain, stress, and energy–density values were calculated more precisely for all reflection peaks of XRD corresponding to the wurtzite hexagonal phase of ZnO in the 20°–100° range from the SSP results. The effect of doping on the optical band-gap was also investigated. The results showed that Mg^{2+} is a good dopant to control some of the ZnO properties, with minimum defects to its structure.

Keywords: D. ZnO; X-ray diffraction; Sol–gel; Strain

1. Introduction

Nanotechnology has the potential to create many new devices with a wide range of applications in the field of medicine [1], electronics [2], and energy production [3]. The increased surface area-to-volume ratios and quantum size effects are the properties that make these materials potential candidates for device applications. These properties can control optical properties such as absorption, fluorescence, and light scattering.

Zinc oxide (ZnO) is an n-type metal oxide semiconductor with a wide band-gap (3.36 eV) and large excitation binding energy. These characteristics make this material interesting for many applications, such as solar cells [4], optical coating [5], and gas sensors [6]. The role of the particle size, doping, impurities, and morphology is very important to these applications, which has driven researchers to focus on the synthesis of doped and pure nanocrystalline ZnO in recent years. Therefore, many methods, including sol–gel [7], combustion [8], precipitation [9], solvothermal [10], microwave [11], spray pyrolysis [12], hydrothermal [13], chemical vapor deposition (CVD) [14], and others, have been developed to prepare ZnO nanostructures and ceramics.

The doping of ZnO with selective elements offers an effective method to enhance and control its electrical and optical properties in nano and ceramic forms. To date, several doped ZnO structures have been fabricated using some of the element cations. For example, Au^{2+} [15], Ce^{3+} [16], Eu^{3+} [17], In^{3+} [18], and Mg^{2+} [19] have been used to control optical properties; Mn^{2+} [20], Cl^{1-} [21], Co^{2+}, Ni^{2+}, Fe^{3+}, Cu^{2+}, and V^{5+} [22] were used to enhance the magnetic properties; and Li^{1+} [23] and Na^{1+} [24] were used to get a p-type form of ZnO. Magnesium-doped ZnO nanoparticles have attracted significant interest in hydrogen production [25], electroluminescence [26], and field effect transistors [27]. Apart from these, synthesis methods that yield different shapes show different optical behaviors. Moreover, since the ionic radii of Mg^{2+} (0.66 Å) and Zn^{2+} (0.74 Å) are quite close, they can alloy by replacing each other in the matrix.

* Corresponding author. Tel.: +60 12 2850849; fax: +60 37 9674146.
E-mail address: alikhorsandzak@gmail.com (A. Khorsand Zak).

0272-8842/$36.00
doi:10.1016/j.ceramint.2011.10.042

In the present work, a simple sol–gel route was created to prepare $Zn_{1-x}Mg_xO$ nanoparticles (NPs) in gelatin media. Gelatin was used as a polymerization agent, serving as a terminator for growing the $Zn_{1-x}Mg_xO$-NPs because it expands during the calcination process and the particles cannot come together easily. The size, morphology, and crystallinity of the resulting $Zn_{1-x}Mg_xO$-NPs were investigated.

2. Experiment

To begin synthesis of Mg-doped ZnO nanoparticles, analytical grade Zinc nitrate hexahydrate ($Zn(NO_3)_2{\cdot}6H_2O$), magnesium nitrate hexahydrate ($Mg(NO_3)_2{\cdot}6H_2O$), gelatin [$(NHCOCH–R_1)_n$, R_1 = amino acid], and distilled water were used as starting materials. In order to prepare 10 g of the final product, the specific amount of zinc and magnesium nitrate were dissolved in 50 mL of distilled water. The quantities of the precursor materials were calculated according to the $Zn_{1-x}Mg_xO$ formula, where $x = 0$, 0.01, 0.03, and 0.05. On the other hand, 8 g of gelatin were dissolved in 300 mL of distilled water, and the solution was stirred at 60 °C. After the gelatin solution became clear, the Zn^{2+} and Mg^{2+} solution were added to the gelatin solution. The container was placed in an oil-bath; meanwhile, the temperature was fixed at 80 °C while continuing to be stirred to obtain a viscose, clear, and honey-like gel. For the calcination process, the gel was rubbed on the inner walls of a crucible, and the crucible was then placed into the furnace. The temperature of the furnace was fixed at 650 °C for 2 h, with a heating rate of 2 °C/min.

The prepared precursor gel of $Zn_{1-x}Mg_xO$-NPs was studied using thermogravimetry analysis (TGA, Q600), and the phase evolutions and structure of the $Zn_{1-x}Mg_xO$-NPs were studied by XRD (Philips, X'pert, CuKα). The TEM observations were carried out on a Hitachi H-7100 electron microscope to examine the shape and particle size of the nanoparticles. The UV–vis spectra were recorded over the range of 350–700 nm by a Lambda 25-Perkin–Elmer UV–vis spectrophotometer.

3. Results and discussion

3.1. TGA

The thermogravimetric and derivative analysis (TGA/DTA) curves of the ZnO-NPs synthesized by the sol–gel method in a gelatin environment are presented in Fig. 1. The TG curve descends until it becomes horizontal at around 500 °C. The TG and DTA traces show three main regions. The first weight loss between 50 and 135 °C (20%) is an initial loss of water—bend Ed_1. The second weight loss from 135 to 220 °C (22%) is attributed to the decomposition of chemically bound groups, which corresponds to bend Ed_2. The third step from 220 to 350 °C (18%) is related to both the decomposition of the organic groups and the formation of the pyrochlore phases—bend Ed_3. The last weight-loss step from 350 to 500 °C (19%) is attributed to the decomposition of the pyrochlore phases, and the formation of ZnO pure phases—bend Ed_4. No weight loss between 500 and 900 °C was detected on the TG curve, which

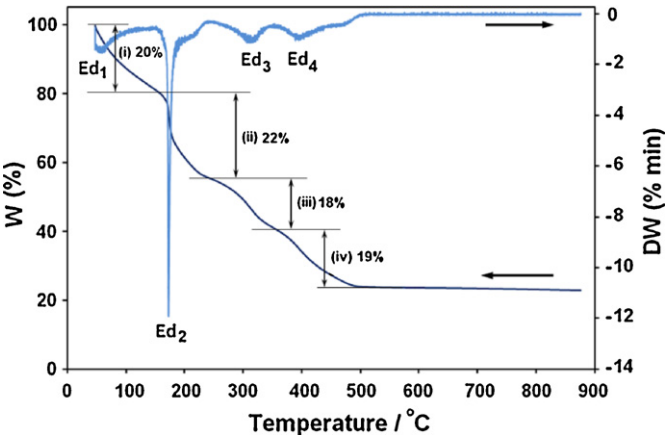

Fig. 1. The TGA curve of the gel from 50 to 900 °C.

indicates the formation of nanocrystalline ZnO as the decomposition product. The TGA of the doped ZnO-NPs were the same, so they were not presented.

3.2. XRD analysis

The XRD patterns of the prepared samples in the range of $2\theta = 20°–100°$ are shown in Fig. 2. All detectable peaks could be indexed as the ZnO wurtzite structure (Ref. Code: 00-005-0664). No further peaks were detected related to Mg, MgO, or other similar compounds. A negligible shift also occurred in peaks for the samples doped with a different amount of Mg in the ZnO matrix compared to the pure ZnO-NPs (Fig. 3). This shift also corresponded to the strain of the compounds and

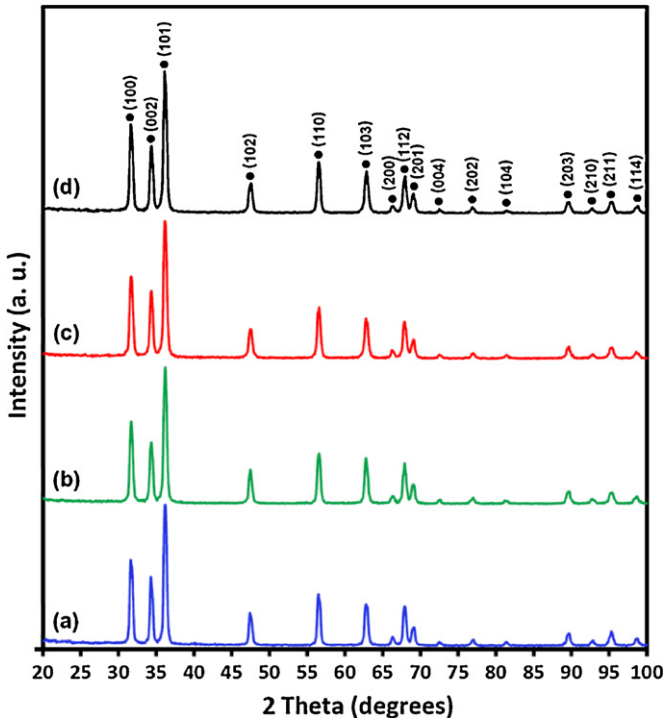

Fig. 2. The XRD pattern of (a) ZnO, (b) $Zn_{0.99}Mg_{0.01}O$, (c) $Zn_{0.97}Mg_{0.03}O$, and (d) $Zn_{0.95}Mg_{0.05}O$.

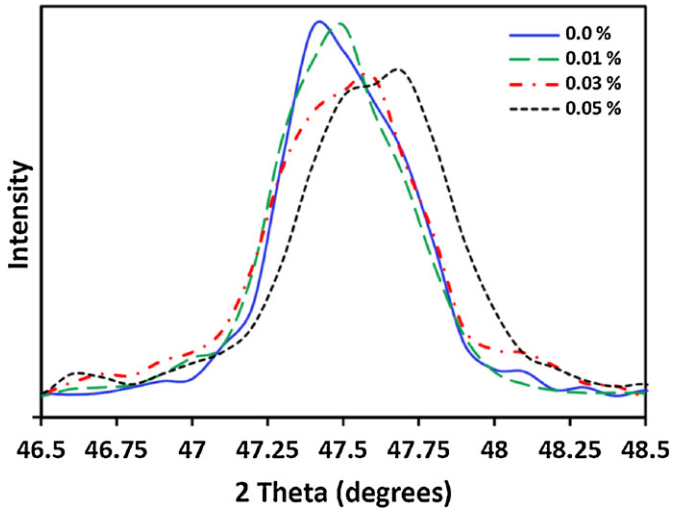

Fig. 3. The (1 0 2) diffraction peak of the samples. The peak was shifted to the higher degrees by increasing the Mg concentration.

replacement of some Zn^{2+} with the Mg^{2+} in each compound due to their different ionic radius.

Wurtzite lattice parameters such as the values of d, the distance between adjacent planes in the Miller indices ($h\ k\ l$) (calculated from the Bragg equation, $\lambda = 2d\sin\theta$), lattice constants a, b, and c, inter-planar angle (the angle φ between the planes ($h_1\ k_1\ l_1$), of spacing d_1 and the plane ($h_2\ k_2\ l_2$) of spacing d_2), and unit cell volumes were calculated using the Lattice Geometry equation [28]. The lattice parameters of the powders calcined at different temperatures are summarized in Table 1.

3.3. Crystalline size and mechanical properties

The crystalline size and mechanical properties of the $Zn_{1-x}Mg_xO$-NPs, $x = 0.0$, 0.01, 0.03, and 0.05, were calculated by the size strain plot method. Normally, the crystalline size of the crystals are determined by the X-ray line broadening method using the Scherrer equation $D = (k\lambda/\beta_D\cos\theta)$, where D is the crystalline size in nanometers, λ is the wavelength of the radiation (1.54056 Å for CuKα radiation), k is a constant equal to 0.94, β_D is the peak width at half-maximum intensity, and θ is the peak position. The breadth of the Bragg peak is a combination of both instrument- and sample-dependent effects. To decouple these contributions, it is necessary to collect a diffraction pattern from the line broadening of a standard material (e.g., silicon) to determine the instrumental broadening. The instrument-corrected broadening β_D corresponding to the diffraction peak of ZnO was estimated using the relation [29]:

$$\beta_D^2 = \left[(\beta^2)_{\text{measured}} - \beta^2_{\text{instrumental}}\right] \Rightarrow \tag{4}$$

$$D = \frac{k\lambda}{\beta_D\cos\theta} \Rightarrow \cos\theta = \frac{k\lambda}{D}\left(\frac{1}{\beta_D}\right) \tag{5}$$

According to previous work, line broadening was essentially isotropic using the Williamson–Hall method [30,31], indicating that the diffracting domains were isotropic and that a micro-strain contribution also occurred. However, in the cases of isotropic line broadening, a better evaluation of the size–strain parameters can be obtained by considering an average size–strain plot (SSP), which gives less weight to data from reflections at high angles, where the precision is usually lower. In this approximation, it is assumed that the crystallite size profile is described by a Lorentzian function and that the strain profile is described by a Gaussian function [32]. Furthermore, the peak broadening that occurred due to the strain is estimated from $\varepsilon \approx \beta_s/\tan\theta$ [28]. The total peak broadening is obtained from the following equation:

$$\beta_{hkl} = \beta_s + \beta_D \tag{6}$$

Accordingly, we obtain:

$$(d_{hkl}\beta_{hkl}\cos\theta)^2 = \frac{A}{D}\left(d^2_{hkl}\beta_{hkl}\cos\theta\right) + \left(\frac{\varepsilon}{2}\right)^2 \tag{7}$$

where A is a constant that depends on the shape of the particles; for spherical particles, it is given as approximately and can be used for the samples. In Fig. 4a–d, the term $(d_{hkl}\beta_{hkl}\cos\theta)^2$ is plotted with respect to $(d_{hkl}{}^2\beta_{hkl}\cos\theta)$ for all orientation peaks of ZnO-NPs with the wurtzite hexagonal phase from $2\theta = 20^\circ$ to 100°. In this case, the crystalline size is determined from the slope of the linearly fitted data, where the root of the y-intercept gives the strain.

According to Hook's law, a linear proportionality between the stress and strain is given as $\sigma = Y\varepsilon$, where σ is the stress of the crystal and Y is the modulus of elasticity, or Young's modulus, for a significantly small strain. This equation deviates from this linear approximation with increasing strain. For a hexagonal crystal, Young's modulus is given by the following relation [33]:

Table 1
The structure parameters of pure and doped ZnO-NPs calcined at 650 °C.

Compound	$2\theta \pm 0.01$	hkl	d_{hkl} (nm) ± 0.0005	Structure	Lattice parameter (nm) ± 0.0005	V (nm^3) ± 0.2	Cos $\varphi \pm 0.002$
ZnO	31.70	(100)	0.2820	Hexagonal	$a = 0.3256$	47.90	0
	34.36	(002)	0.2608		$c = 0.5216$		
$Zn_{0.99}Mg_{0.01}O$	31.71	(100)	0.2820	Hexagonal	$a = 0.3256$	47.88	0
	34.37	(002)	0.2607		$c = 0.5215$		
$Zn_{0.97}Mg_{0.03}O$	31.70	(100)	0.2821	Hexagonal	$a = 0.3257$	47.90	0
	34.38	(002)	0.2607		$c = 0.5214$		
$Zn_{0.95}Mg_{0.05}O$	31.70	(100)	0.2821	Hexagonal	$a = 0.3257$	47.90	0
	34.38	(002)	0.2606		$c = 0.5212$		

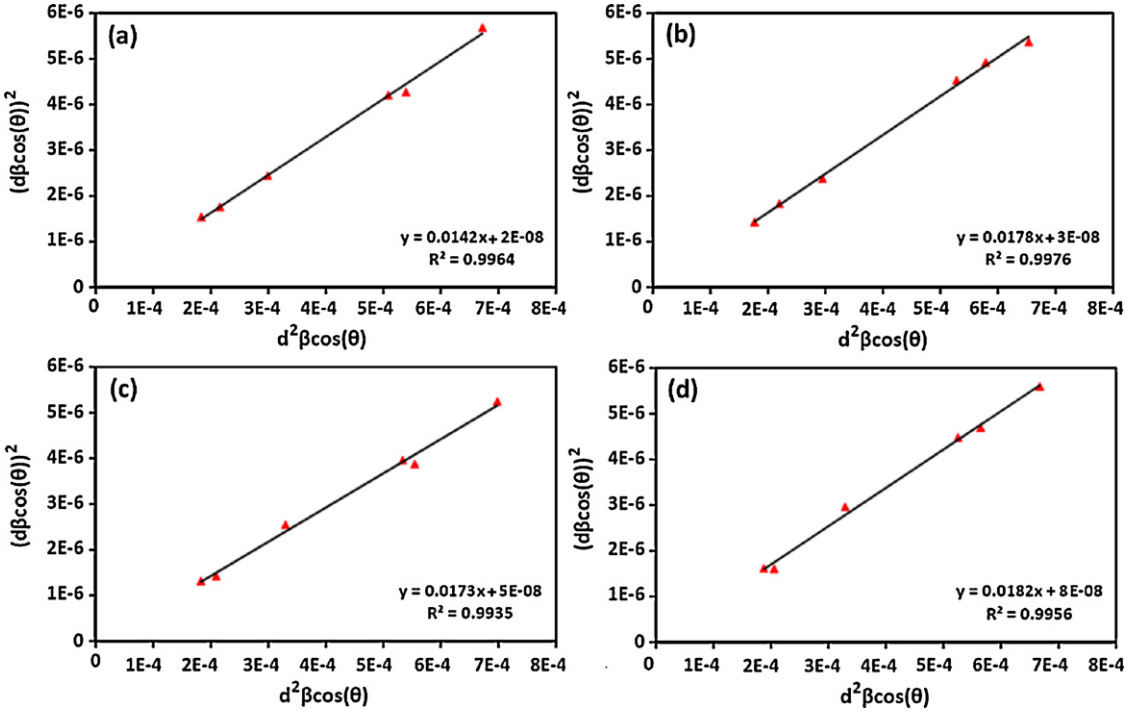

Fig. 4. The SSP plot of (a) ZnO, (b) $Zn_{0.99}Mg_{0.01}O$, (c) $Zn_{0.97}Mg_{0.03}O$, and (d) $Zn_{0.95}Mg_{0.05}O$. The particle size is achieved from the slope of the linearly fitted data while the root of the *y*-intercept gives the strain.

$$Y_{hkl} = \frac{\left[h^2 + \frac{(h+2k)^2}{3} + \left(\frac{al}{c}\right)^2\right]^2}{s_{11}\left(h^2 + \frac{(h+2k)^2}{3}\right)^2 + s_{33}\left(\frac{al}{c}\right)^4 + (2s_{13} + s_{44})\left(h^2 + \frac{(h+2k)^2}{3}\right)\left(\frac{al}{c}\right)^2} \quad (8)$$

where s_{11}, s_{13}, s_{33}, and s_{44} are the elastic compliances of ZnO with values of 7.858×10^{-12}, -2.206×10^{-12}, 6.940×10^{-12}, and 23.57×10^{-12} m^2 N^{-1}, respectively [34]. Young's modulus for the $Zn_{1-x}Mg_xO$-NPs was calculated, and the stress was then calculated according to Eq. (7). For an elastic system that follows Hooke's law, the energy density u (energy per unit) can be calculated from $u = (\varepsilon^2 Y_{hkl})/2$. The results obtained from the SSP models are summarized in Table 2.

Table 2
Geometric parameters of pure and doped ZnO-NPs calcined at 650 °C.

Compound	Method				
	Size–strain plot				
	D (nm)	$\varepsilon \times 10^{-4}$	$Y \times 10^9$	$\sigma \times 10^6$	$u \times 10^3$
ZnO	52.82	2.83	146	41.32	5.85
$Zn_{0.99}Mg_{0.01}O$	42.13	3.46	146	50.50	8.74
$Zn_{0.97}Mg_{0.03}O$	43.35	4.90	146	71.54	17.53
$Zn_{0.95}Mg_{0.05}O$	41.21	5.66	146	82.64	23.39

3.4. Morphology study of the ZnO-NPs

Fig. 5a–d shows the TEM morphology of the $Zn_{1-x}Mg_xO$-NPs ($x = 0.0$, 0.01, 0.03, and 0.05) calcined at temperature of 650 °C for 2. The corresponding size distribution histograms of the TEM micrographs are presented below. The results of TEM show that the particle sizes of the ZnO-NPs decreased with Mg^{2+} doping. The changes in particle sizes are negligible; according to the histograms, they were about 15% compared to the pure ZnO-NPs. This can possibly be related to the decreasing of the self-assembly of the crystals due to the impurities defects. The histograms indicate that the main particle sizes of the $Zn_{1-x}Mg_xO$-NPs ($x = 0.0$, 0.01, 0.03, and 0.05) calcined at temperatures of 650 °C were approximately 52 ± 14, 46 ± 10, 40 ± 9, and 41 ± 10 nm, respectively.

3.5. UV–vis diffuse absorbance spectra and band-gap

The UV–vis absorbance spectra of the $Zn_{1-x}Mg_xO$-NPs ($x = 0.0$, 0.01, 0.03, and 0.05) calcined at a temperature of 650 °C for 2 h are shown in the inset of Fig. 6. The relevant decrease in the absorbance at wavelengths greater than 350 nm

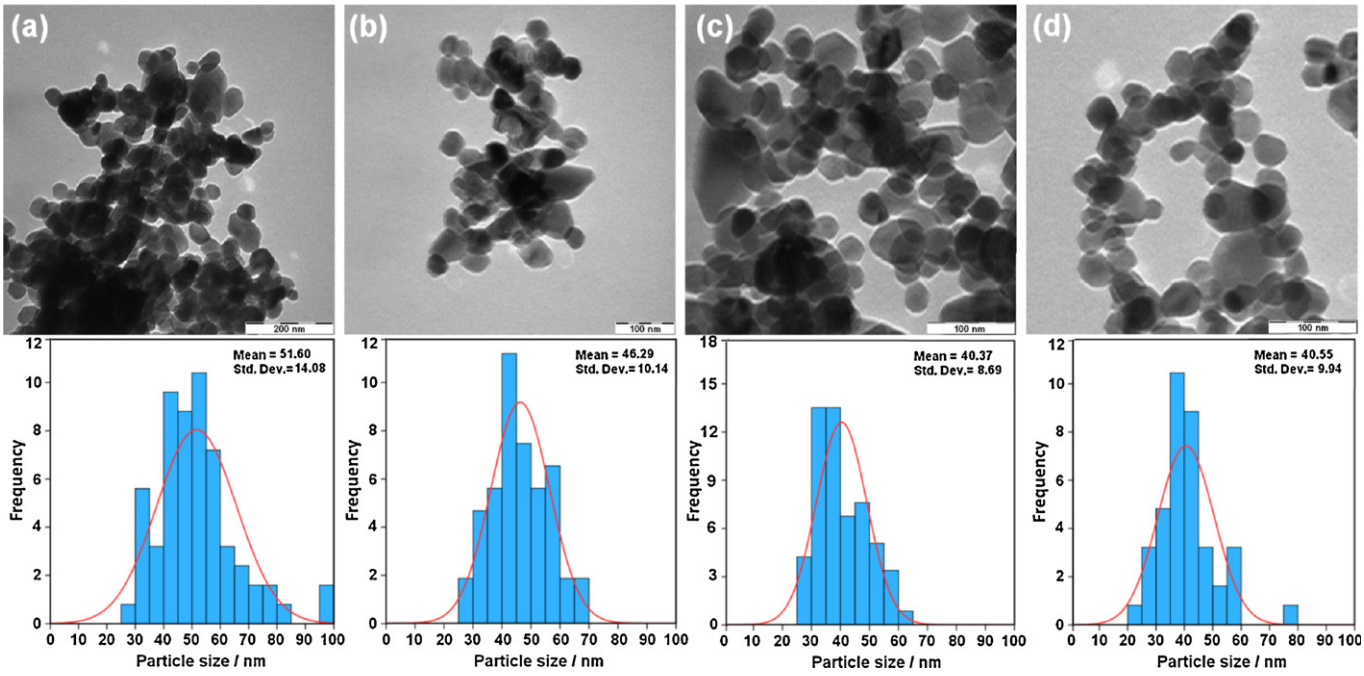

Fig. 5. The TEM micrograph of (a) ZnO, (b) $Zn_{0.99}Mg_{0.01}O$, (c) $Zn_{0.97}Mg_{0.03}O$, and (d) $Zn_{0.95}Mg_{0.05}O$. The size distributions are presented below the TEMs.

can be assigned to the intrinsic band-gap absorbance of ZnO due to the electron transitions from the valence band to the conduction band ($O_{2p} \rightarrow Zn_{3d}$) [35]. Interestingly, an obvious red-shift in the absorbance edge was observed for the products with different percentages of the dopant. This might be due to changes in their morphologies, particle size, and surface microstructures. Moreover, the direct band-gap energies estimated from a plot of $(\alpha \times h\nu)^2$ versus the photo energy ($h\nu$) according to the Kubelka–Munk model [36], as shown in Fig. 5, were 3.29, 3.30, 3.34, and 3.36 eV for the $Zn_{1-x}Mg_xO$-NPs ($x = 0.0$, 0.01, 0.03, and 0.05) calcined at temperature of 650 °C for 2 h, where α (*absorption*) is calculated using $A = l \times C \times \alpha$ (l is the thickness and C is the concentration of material). Such an increase in the ZnO band-gap energy is in good agreement with the corresponding red-shift seen in the previously mentioned absorbance edge. As obtained from the TEM results, the particle size decreased with the addition of the dopant to the structure. Decreasing the doped ZnO-NPs particle sizes caused an increase in the band-gap.

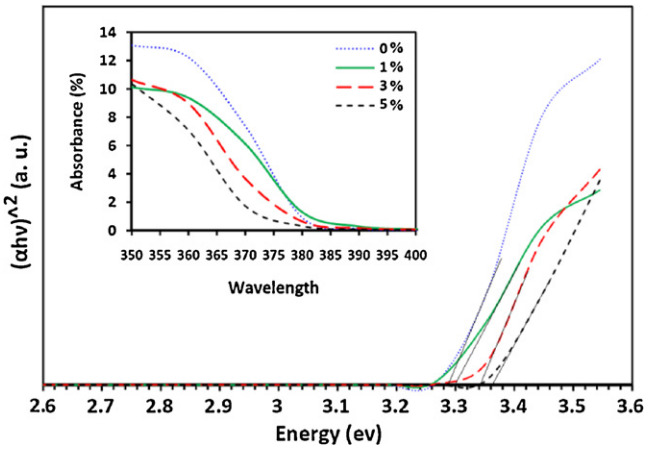

Fig. 6. The UV–vis spectrum of the $Zn_{1-x}Mg_xO$ ($X = 0.0$, 0.01, 0.03, and 0.05).

4. Conclusion

The $Zn_{1-x}Mg_xO$-NPs ($x = 0.0$, 0.01, 0.03, and 0.05) were synthesized by a simple sol–gel method using gelatin as a stabilizer and polymer agent. The prepared gel was calcined at a temperature of 650 °C for 2 h to get a fine powder, free of organic phases. The XRD patterns proved the formation of the hexagonal structure, and no extra phases were detected. The crystalline sizes of the nanoparticles were calculated using the SSP method, considering the strain of the particles using the XRD results. The crystalline sizes of 52 ± 2, 42 ± 2, 43 ± 2, and 41 ± 2 were calculated for $Zn_{1-x}Mg_xO$-NPs, ($x = 0.0$, 0.01, 0.03, and 0.05), respectively. TEM results showed that the particle size was decreased with the doping of Magnesium, and the sizes of $Zn_{1-x}Mg_xO$-NPs ($x = 0.0$, 0.01, 0.03, and 0.05) were obtained as 52 ± 14, 46 ± 10, 40 ± 9, and 41 ± 10 nm, respectively. The results of UV–vis spectroscopy showed that the band-gap of the $Zn_{1-x}Mg_xO$-NPs was increased with dopant increases. The estimated band-gaps for $Zn_{1-x}Mg_xO$-NPs ($x = 0.0$, 0.01, 0.03, and 0.05) were 3.29, 3.30, 3.34, and 3.36 eV. All of these results indicate that the Mg^{2+} is a suitable dopant to control the properties of ZnO-NPs.

Acknowledgments

This work was supported by the University of Malaya through grants no: UM.C/625/1/HIR/041.

References

[1] V. Wagner, A. Dullaart, B. Anne-Katrin, A. Zweck, The emerging nanomedicine landscape, Nat. Biol. Technol. 24 (2006) 1211–1217.

[2] F.A. Buot, Mesoscopic physics and nanoelectronics: nanoscience and nanotechnology, Phys. Rep. 234 (1993) 73–174.

[3] S.Y. Huang, G. Schlichthorl, A.J. Nozik, M. Gratzel, A.J. Frank, Charge recombination in dye-sensitized nanocrystalline TiO_2 solar cells, J. Phys. Chem. B 101 (1997) 2576–2582.

[4] L. Lu, R. Li, K. Fan, T. Peng, Effects of annealing conditions on the photoelectrochemical properties of dye-sensitized solar cells made with ZnO nanoparticles, Sol. Energy 84 (2010) 844–853.

[5] P. Prepelita, R. Medianu, B. Sbarcea, F. Garoi, M. Filipescu, The influence of using different substrates on the structural and optical characteristics of ZnO thin films, Appl. Surf. Sci. 256 (2010) 1807–1811.

[6] J.H. Lee, Gas sensors using hierarchical and hollow oxide nanostructures: overview, Sens. Actuators B 140 (2009) 319–336.

[7] A.K. Zak, W.H. Majid Abd., M. Darroudi, R. Yousefi, Synthesis and characterization of ZnO nanoparticles prepared in gelatin media, Mater. Lett. 65 (2011) 70–73.

[8] A.K. Zak, M.E. Abrishami, W.H. Majid Abd., R. Yousefi, S.M. Hosseini, Effects of annealing temperature on some structural and optical properties of ZnO nanoparticles prepared by a modified sol–gel combustion method, Ceram. Int. 37 (2011) 393–398.

[9] R. Song, Y. Liu, L. He, Synthesis and characterization of mercaptoacetic acid-modified ZnO nanoparticles, Solid State Sci. 10 (2008) 1563–1567.

[10] P. Tonto, O. Mekasuwandumrong, S. Phatanasri, V. Pavarajarn, P. Praserthdam, Preparation of ZnO nanorod by solvothermal reaction of zinc acetate in various alcohols, Ceram. Int. 34 (2008) 57–62.

[11] T. Thongtem, A. Phuruangrat, S. Thongtem, Characterization of nanostructured ZnO produced by microwave irradiation, Ceram. Int. 36 (2010) 257–262.

[12] O. Milošević, B. Jordović, D. Uskoković, Preparation of fine spherical ZnO powders by an ultrasonic spray pyrolysis method, Mater. Lett. 19 (1994) 165–170.

[13] A.A. Ismail, A. El-Midany, E.A. Abdel-Aal, H. El-Shall, Application of statistical design to optimize the preparation of ZnO nanoparticles via hydrothermal technique, Mater. Lett. 59 (2005) 1924–1928.

[14] R. Yousefi, M.R. Muhamad, A.K. Zak, The effect of source temperature on morphological and optical properties of ZnO nanowires grown using a modified thermal evaporation set-up, Curr. Appl. Phys. 11 (2011) 767–770.

[15] N. Hongsith, C. Viriyaworasakul, P. Mangkorntong, N. Mangkorntong, S. Choopun, Ethanol sensor based on ZnO and Au-doped ZnO nanowires, Ceram. Int. 34 (2008) 823–826.

[16] G. Achamma, K.S. Suchinder, C. Santa, M.M. Malik, M.S. Qureshi, Detailed X-ray diffraction and photoluminescence studies of Ce doped ZnO nanocrystals, J. Alloys Compd. 509 (2011) 5942–5946.

[17] Yunlong Yu, Daqin Chen, Ping Huang, Hang Lin, Yuansheng Wang, Structure and luminescence of Eu^{3+} doped glass ceramics embedding ZnO quantum dots, Ceram. Int. 36 (2010) 1091–1094.

[18] R. Yousefi, M.R. Muhamad, A.K. Zak, Investigation of indium oxide as a self-catalyst in ZnO/ZnInO heterostructure nanowires growth, Thin Solid Films 518 (2010) 5971–5977.

[19] R. Yousefi, M.R. Muhamad, Effects of gold catalysts and thermal evaporation method modifications on the growth process of $Zn_{1-x}Mg_xO$ nanowires, J. Solid State Chem. 183 (2010) 1733–1739.

[20] O.D. Jayakumar, I.K. Gopalakrishnan, C. Sudakar, R.M. Kadam, S.K. Kulshreshth, Significant enhancement of room temperature ferromagnetism in surfactant coated polycrystalline Mn doped ZnO particles, J. Alloys Compd. 438 (2007) 258–262.

[21] R. Yousefi, A.K. Zak, M.R. Mahmoudian, Growth and characterization of Cl-doped ZnO hexagonal nanodisks, J. Solid State Chem. 184 (2011) 2678–2682.

[22] J.M. Wesselinowa, A.T. Apostolov, A possibility to obtain room temperature ferromagnetism by transition metal doping of ZnO nanoparticles, J. Appl. Phys. 107 (2010) 053917.

[23] B.Y. Zhang, B. Yao, Y.F. Li, Z.Z. Zhang, B.H. Li, C.X. Shan, D.X. Zhao, D.Z. Shen, Investigation on the formation mechanism of *p*-type Li-N dual-doped ZnO, Appl. Phys. Lett. 97 (2010) 222101.

[24] C. Wu, L. Shen, Q. Huang, Y.C. Zhang, Synthesis of Na-doped ZnO nanowires and their antibacterial properties, Powder Technol. 205 (2011) 137–142.

[25] X. Deng, J. Sun, S. Yu, J. Xi, W. Zhu, X. Qiu, Steam reforming of ethanol for hydrogen production over $NiO/ZnO/ZrO_2$ catalysts, Int. J. Hydrogen Energy 33 (2008) 1008–1013.

[26] D. Wei Wang, Su-Ling Zhao, Zheng Xu, Chao Kong, Wei Gong, The improvement of near-ultraviolet electroluminescence of ZnO nanorods/MEH–PPV heterostructure by using a ZnS buffer layer, Org. Electron. 12 (2011) 92–97.

[27] W.K. Hong, S. Song, D.K. Hwang, S.S. Kwon, G. Jo, S.J. Park, T. Lee, Effects of surface roughness on the electrical characteristics of ZnO nanowire field effect transistors, Appl. Surf. Sci. 254 (2008) 7559–7564.

[28] B.D. Cullity, Elements of X-ray Diffraction, Addison-Wesley Publishing Company Inc, California, 1956.

[29] K.D. Rogers, P. Daniels, Biomaterial 23 (2002) 2577.

[30] A.K. Zak, W.H. Majid Abd., M.E. Abrishami, R. Yousefi, X-ray analysis of ZnO nanoparticles by Williamson–Hall and size–strain plot methods, Solid State Sci. 13 (2011) 251.

[31] R. Yogamalar, R. Srinivasan, A. Vinu, K. Ariga, A.C. Bose, X-ray peak broadening analysis in ZnO nanoparticles, Solid State Commun. 149 (2009) 1919.

[32] M.A. Tagliente, M. Massaro, Strain-driven (0 0 2) preferred orientation of ZnO nanoparticles in ion-implanted silica, Nucl. Ins. Meth. In. Phys. Res. B 266 (2008) 1055.

[33] J. Zhang, Y. Zhang, K.W. Xu, V. Ji, General compliance transformation relation and applications for anisotropic hexagonal metals, Solid State Commun. 139 (2006) 87.

[34] J.F. Nye, Physical Properties of Crystals: Therir Representation by Tensors and Matrices, Oxford, New York, 1985.

[35] H. Yu, J. Yu, B. Cheng, M. Zhou, Effects of hydrothermal post-treatment on microstructures and morphology of titanate nanoribbons, J. Solid State Chem. 179 (2006) 349–354.

[36] J. Yu, C. Li, S. Liu, Effect of PSS on morphology and optical properties of ZnO, J. Colloid Interface Sci. 326 (2008) 433–438.